Precision Engineering 90 (2024) 71–80

Contents lists available at ScienceDirect

Precision Engineering

journal homepage: www.elsevier.com/locate/precision

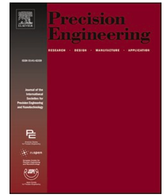

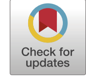

Ion beam smoothing of fused silica at atomic-scale assisted by damage recovery using inductively coupled plasma

Bing Wu [a,1], Shaoxiang Liang [a,1], Junqi Zhang [a], Xuemiao Ding [c], Tom Chiu [c], Pei Huang [a], Yinhui Wang [a,b,*], Hui Deng [a,b,**]

[a] Department of Mechanical and Energy Engineering, Southern University of Science and Technology, Shenzhen, Guangdong 518055, PR China

[b] Shenzhen Engineering Research Center for Semiconductor-specific Equipment, Department of Mechanical and Energy Engineering, Southern University of Science and Technology, Shenzhen, Guangdong 518055, PR China

[c] Boffotto Semiconductor Limited, No.118 Dongcheng Road, Hongqi Town, Zhuhai City, Guangdong Province, PR China

ARTICLE INFO

Handling Editor: Prof. R. Leach

Keywords:
Fused silica
Plasma-induced atom migration manufacturing
Ion beam figuring
Subsurface damage
Atomically smooth

ABSTRACT

For conventional optical manufacturing combining ion beam figuring (IBF) and abrasive finishing, it is difficult to achieve an atomic-scale smooth surface with microroughness below 0.1 nm. Because the abrasives inevitably damage the surface, and the damages are exposed during ion sputtering. To solve this problem, plasma-induced atom migration manufacturing (PAMM) and IBF were combined in this study. PAMM is a damage recovery process based on atom migration effect. In this study, PAMM was employed to recover the subsurface damage and then the damage-less surface was further processed by IBF to remove the form error as well as reduce the roughness to atomic level. Full spatial frequency error convergence was achieved via the combined process of PAMM and IBF. A good surface accuracy of 3.89 nm RMS and an atomically smooth surface with a roughness of 0.044 nm were obtained. The less damage characteristic of the hybrid process was also demonstrated by buffered oxide etching (BOE). This study proposed and verified a hybrid process combining PAMM for damage recovery and IBF for figuring and atomic-scale smoothing, which provided a novel process strategy for manufacturing ultra-precision optics with high quality.

1. Introduction

Fused silica-based optical elements are widely used in semiconductor lithography systems for reflecting light [1,2]. The good surface quality is essential in improving lithography performance [3,4]. Some stringent requirements for the optical surface have been put forward, such as nanometer-level precision, atomic-scale smoothness, and less subsurface damage (SSD) [5–7]. The surface errors can be divided into three different regions based on spatial frequency: low-spatial frequency (LSF), mid-spatial frequency (MSF), and high-spatial frequency (HSF) errors [8]. These spatial frequency errors jointly affect the performance of optical elements. For example, the LSF errors directly induce wavefront aberrations [9], and the HSF roughness is regarded as the loss mechanism in extreme ultraviolet (EUV) light by high-angle scattering [10,11].

Generally, ultra-precision mirrors are fabricated via grinding, polishing, and numerically controlled figure correction machining [12]. The LSF form errors are corrected by controlling the dwell time of a machining tool, such as magnetorheological finishing (MRF) [13], elastic emission machining (EEM) [14], fluid jet polishing (FJP) [15,16], and ion beam figuring (IBF) [17]. Among them, IBF is a highly deterministic manufacturing process with the advantage of atomic-level material removal by physical sputtering effect [18,19]. A root-mean-square (RMS) figure accuracy of 0.13 nm was achieved over a diameter of 178 mm of spherical mirrors [16]. Thus, IBF is a well-developed process for correcting LSF surface errors and widely used as the final figuring process [20].

However, the effect of ion beam sputtering on surface roughness is strongly related to the initial surface quality [21]. During grinding and polishing processes, the scratches and SSD of fused silica mirrors were easily generated [22], such as micro-cracks and amorphous layer, which would seriously influence the subsequent atomic/molecular material

* Corresponding author.
** Corresponding author.
E-mail addresses: wangyh3@sustech.edu.cn (Y. Wang), dengh@sustech.edu.cn (H. Deng).
[1] The authors contribute equally to this paper.

https://doi.org/10.1016/j.precisioneng.2024.08.003
Received 29 April 2024; Received in revised form 24 July 2024; Accepted 6 August 2024
Available online 8 August 2024
0141-6359/© 2024 Elsevier Inc. All rights are reserved, including those for text and data mining, AI training, and similar technologies.

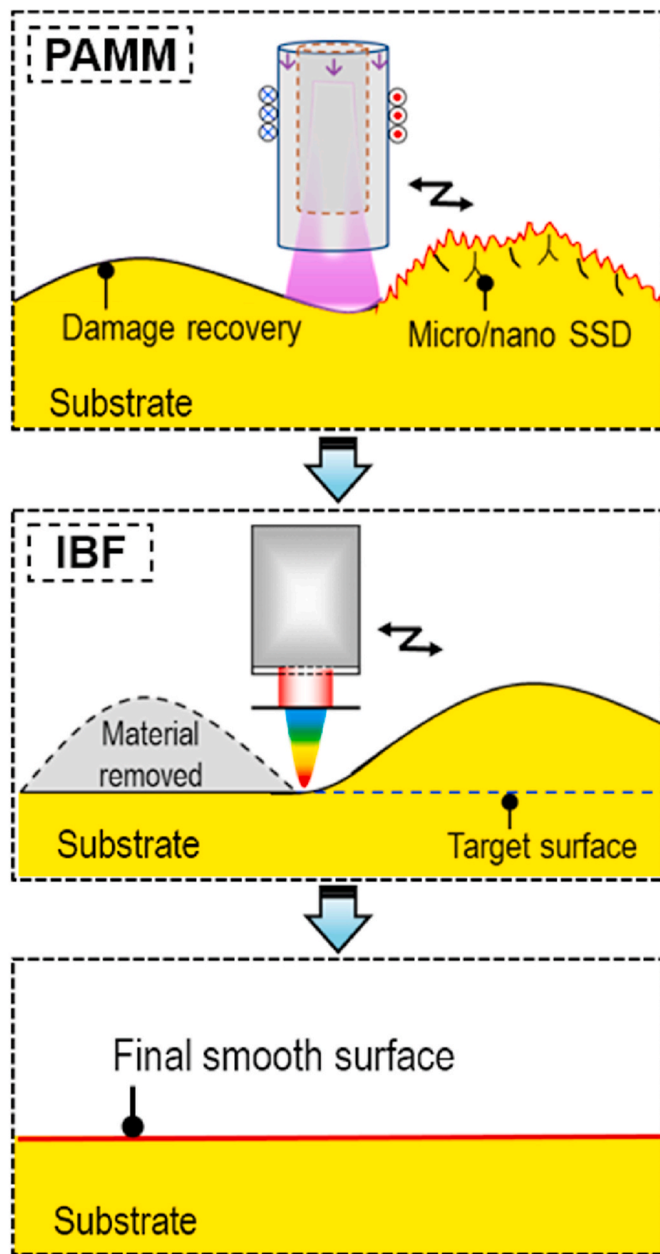

Fig. 1. Schematic view of PAMM and IBF processes of fused silica.

removal process [23]. Xu et al. reported that surface defects with different properties and structures display different evolution laws during ion beam sputtering. The evolution of brittle scratches indicated that the scratch depth was increased from 89 to 248 nm, and a large pit was formed, which seriously deteriorated the surface roughness and form accuracy of IBF [24]. Savvides revealed that the roughness of the substrates with a deep SSD layer degraded from 0.496 to 0.570 nm, and several large holes were formed after ion beam sputtering. In contrast, the roughness of the super-polished sample with a minimal SSD layer did not change (~0.1 nm) [25].

Various methods are developed to remove the scratches and SSD generated during grinding and polishing, such as HF etching, chemical mechanical polishing (CMP), and MRF [26–29]. HF etching can effectively expose the SSD and remove the defects layer, but the existence of etching pits deteriorates the surface quality. CMP and MRF involve abrasives in contact with the surface, and nanoscale damage is inevitably induced by mechanical effects. For example, an amorphous layer is induced due to the use of abrasives in CMP, though an ultrasmooth

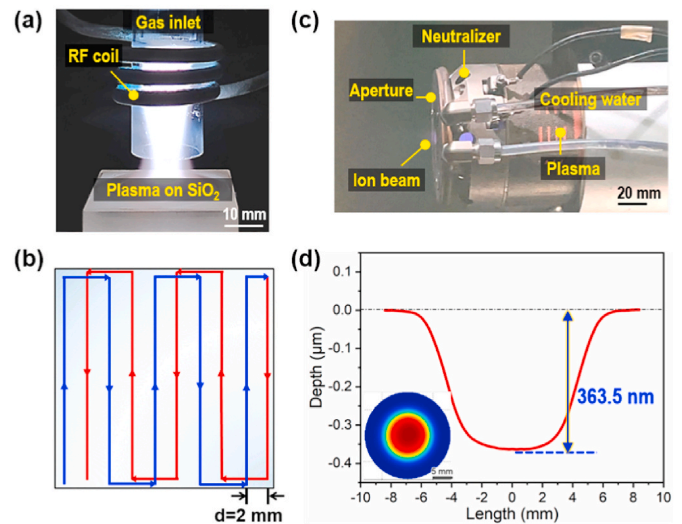

Fig. 2. (a) Photograph of the plasma device. (b) Photograph of the ion source device. (c) Schematic of the plasma scanning route. (d) Removal footprint and cross-sectional profile of the IBF.

Table 1
Conditions for PAMM of fused silica.

Parameters	values
Substrate	Fused silica: 40 × 40 × 10 mm^3, CMP processed
Flow rate of Ar	Ignition gas: 1.5 slm
	Cooling gas: 18.0 slm
RF power	1200 W
Working distance	15 mm
Scanning step/speed	2 mm/80 mm/min
Scanning time	12 min

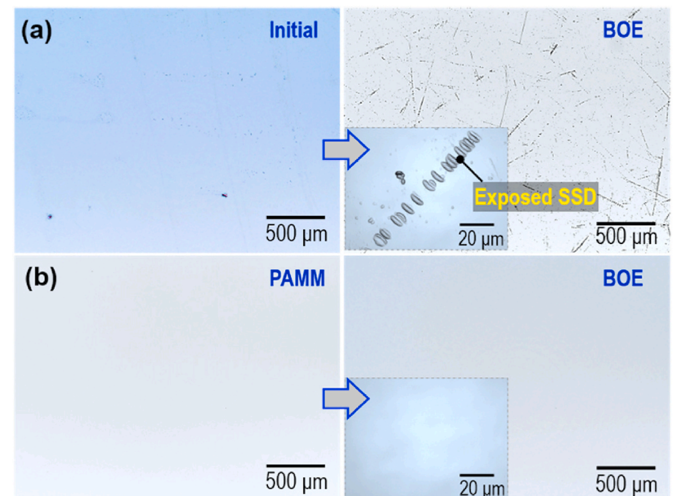

Fig. 3. Surface topography of fused silica before and after dipping in BOE solution for 10 min. (a) Initial surface (CMP processed). (b) PAMM processed surface.

surface with *S*a roughness of 0.13 nm can be obtained [30].

Recently, plasma-induced atom-migration manufacturing (PAMM) was developed to recover rather than remove the SSD for fused silica surfaces [31,32]. Atmospheric pressure inductively coupled plasma (ICP) with high temperature and high radical density was used for the PAMM process. It can rapidly realize damage recovery and atomic-level smoothing of the fused silica surface by the migration of atoms from

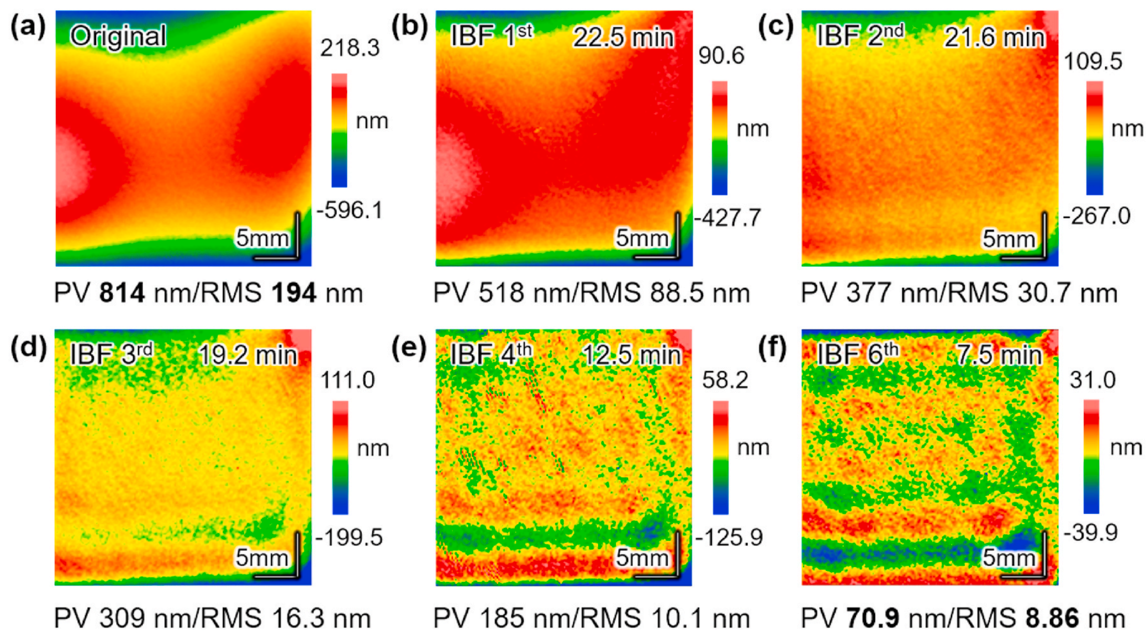

Fig. 4. The LI image, form error (PV, RMS) and processing time of original surface and IBF processed surface by different cycles.

peaks to valleys. Unlike the conventional subtractive manufacturing technology, PAMM hardly removes any material. The scratches with micrometer dimensions can be effectively recovered to an ultrasmooth surface. Moreover, the roughness of a ground silica surface was drastically reduced from *S*a 391 nm to *S*a 0.16 nm within 10 min [32]. Thus, PAMM effectively recovers surface damage and decreases surface HSF errors to the atomic level. Considering the damage recovery and atomic-level smoothing ability of PAMM, it can be combined with IBF to improve surface quality. Moreover, the effect of damage recovered surface through PAMM on the performance of IBF has not yet been reported.

This paper combines PAMM with IBF for achieving nanometer-level precision, atomic-scale smoothness, and less subsurface damage of optical surface. The damage recovery property of PAMM was demonstrated. The IBF process was conducted on the initial fused silica surfaces with scratches, and the evolution of different spatial frequency errors was analyzed. Then, the PAMM-IBF manufacturing process was conducted to complete the convergence limit of different spatial frequency errors. The surface quality after PAMM-IBF was further evaluated. This paper thus provides a new strategy for manufacturing ultra-precision optics.

2. Experimental methods

Fig. 1 shows the schematic view of the proposed PAMM-IBF process of fused silica. The original fused silica substrates are processed by CMP. Due to the plastic deformation-based material removal mechanism, micro/nanoscale defects are inevitably introduced to the surface and subsurface [33]. These defects cannot be removed and will affect the subsequent IBF process. Thus, PAMM is used to recover scratches and the SSD layer, which is a physical migration process. Moreover, an atomic-scale smooth surface can be obtained after PAMM. Then, IBF is conducted to correct the surface form errors to nanometer-level precision. It is expected that surface roughness can be maintained or even reduced during IBF since PAMM has recovered the damaged layer.

The photograph in Fig. 2(a) presents the plasma torch for PAMM processing on a fused silica substrate. The PAMM setup comprises a radio frequency power, a matcher, a copper inductor coil, a quartz torch, and a three-axis numerical controlled platform. During the PAMM process, only high-purity Ar gas was supplied through the inner and outer quartz tubes. The plasma was set in raster scanning mode to realize the whole surface polishing of the fused silica surfaces. The scanning route is shown in Fig. 2(b), and the step pitch is 2 mm. In the PAMM process, the radio frequency power was constant at 1200 W, corresponding to an average temperature of 1331 K over the plasma region, consistent with our previous research results [31]. The processing parameters of PAMM are shown in Table 1.

Fig. 2(c) shows the photograph of the ion source device for the IBF processing. The IBF setup consists of vacuum, motion, and ion source systems. In the ion source, Ar plasma is ignited by RF power and a matcher, and the ions are extracted and accelerated from plasma into a beam through focusing grids. The ion beam transfers energy to the sample surface, and these atoms in the surface escape after gaining enough energy, so the material removal occurs. The neutralizer is used to neutralize residual ions on the substrate surface. Aperture with different dimensions can adjust the size of the ion beam. As shown in Fig. 2(d), a Gaussian-shaped and rotationally symmetrical removal footprint was obtained by IBF with a 10 mm aperture. From the cross-section profile, the removal depth reached 363.5 nm after ion beam sputtering. The static duration was 60 s with a power of 120 W, a working distance of 15 mm, a voltage of 800 V, and an Ar flow rate of 6 sccm. The volume removal rate (VRR) reached 0.023 mm^3/min. Similar to other optical figuring techniques, the critical process of IBF is the calculation algorithm of dwell time. A two-dimensional convolution model can describe the calculation process based on the removal function and amount of removal material [34]. Then, the dwell time is transformed into the processing speed control code for the figuring process.

Commercially available fused silica with the dimension of 40 × 40 × 10 mm^3 was mainly utilized in the experiments. All samples were ultrasonically cleaned with high-purity alcohol (99.5 %) and deionized water and then dried with nitrogen gas (99.999 %). Buffer oxide etching (BOE) solution was utilized to expose the subsurface damage of substrates, similar to our previous study [35]. The ion beam figuring experiments were conducted on IFS1000–600B equipment (*ÅFiSy* Technology). The form errors of the silica surfaces before and after figuring were measured by a laser interferometer (LI, *Tyggo* INF150V-LP). The surface roughness of MSF and HSF errors was measured by scanning white light interferometry (SWLI, *Taylor* Hobson CCI) and atomic force microscope under tapping mode (AFM, *Bruker*

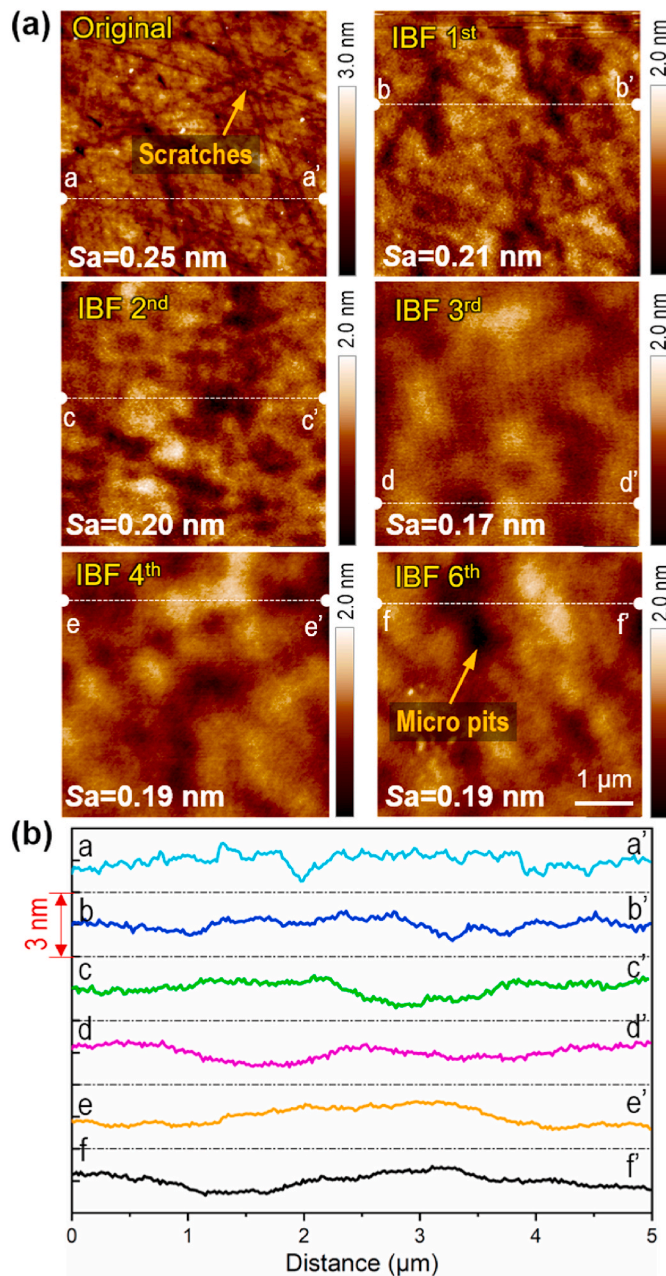

Fig. 5. The roughness (a) and profiles (b) of the original surface and IBF processed surface by different cycles.

Dimension Edge), respectively. Power spectral density (PSD) was utilized to evaluate the surface errors in a wide spatial frequency range. The overall surface images were confirmed by a laser scanning confocal microscope (LSCM, *Keyence* VK-X100).

3. Results and discussion

3.1. Damage recovery of PAMM

A commercially available fused silica sample is usually accompanied by an SSD layer, which is difficult to observe due to the polishing redeposition layer on the surface. The original samples were etched for 10 min in the BOE solution to expose the defects. The LSCM images of the original surface and after etching in BOE solution are shown in Fig. 3 (a). Although the initial surface was smooth without scratches, many defects with linear and pot characteristics were exposed on the surface after BOE, indicating the SSD layer on the original surface. From the inset, the typical Hertz scratches can be seen clearly.

In contrast, the LSCM images of the PAMM polished and then BOE etched surfaces are shown in Fig. 3(b). After PAMM, the surface was very smooth without scratches. After immersion in BOE solution, a smooth surface without defects can be identified, which demonstrated that PAMM recovered the scratches and SSD layer. The atomic-scale mechanism of damage recovery was clarified as the atomic migration effect by molecular dynamics simulation [31]. The migration process included bond breaking, atom adsorption, atom movement, and bond formation. With absorbing enough energy from plasma, the covalent bonds between Si and O atoms cleave, which results in generating free atoms or atomic clusters. These free atoms and clusters are adsorbed on the surface only by van der Waals interactions, and tend to migrate to low energy sites based on the principle of energy minimization. With the free atoms and clusters in the peak positions filling the low pit position in the surface, the surface energy decreases. Then, these free atoms and clusters form covalent bonds. This migration process continues until an ultrasmooth surface realized, which is equivalent to atomic rearrangement on the fused silica surface [31]. Thus, the defects on the original surface/subsurface can be almost completely recovered, and a smooth surface can be obtained by PAMM.

3.2. IBF of fused silica

IBF was conducted on a fused silica sample under several processing cycles. In this work, the sample's surface topography and form error were analyzed after each processing cycle. The processing time of each cycle was also recorded to evaluate the efficiency. After six cycles of IBF processing, the surface form error hardly reduces. This is because the 10 mm aperture limits the accuracy of the figuring. As shown in Fig. 4(a), it exhibits obvious form errors on the original sample, and the value of peak-to-valley (PV) is 814 nm, and RMS is 194 nm. After two IBF processing cycles, as shown in Fig. 4(c), the form error was reduced to PV of 377 nm and RMS of 30.7 nm within 44.1 min. The processing time for the higher-order processing cycle became shorter. However, the convergence rate for reducing the form error decreases with more processing cycles. The processing time of the 6th cycle only consumed 7.5 min, as shown in Fig. 4(f), and the RMS value of the surface decreased to 8.86 nm. As far as processing efficiency and precision are concerned, IBF is an effective technology that can converge the LSF form error with nanometer-level precision.

Besides the form error, the surface roughness is also a significant evaluation index of the processed surfaces during IBF processing. The surface topography for the sample in various stages is shown in Fig. 5(a) by AFM observation. It can be seen that the roughness of *Sa* is 0.25 nm for the original surface, and there are microscopic scratches on its surface. With the continuous material removal during multiple cycles of processing of IBF, the scratches gradually evolved to micro pits, and the roughness decreased to 0.19 nm of *Sa*. However, it seems difficult to further decrease to sub-angstrom level of the roughness due to pit structure. The final forming surface's pit structure was considered the original subsurface damage at micro/nano scale [25]. With the material removal for ion beam sputtering, the damage gradually evolved into these micro/nano pit structures. IBF cannot further remove these micro pits. The profile changes for the surfaces in Fig. 5(a) are shown in Fig. 5 (b). It can be seen that the scratch width increased gradually, and a large pit profile formed.

IBF completed the efficient convergence of surface form error from hundreds of nanometers to nanometers and simultaneously reduced the *Sa* roughness to around 0.2 nm. The limitation of roughness is considered to be the surface micro-damage of the original sample. Owing to the damage recovery and smoothing advantages of PAMM, it was combined with IBF to improve the surface quality.

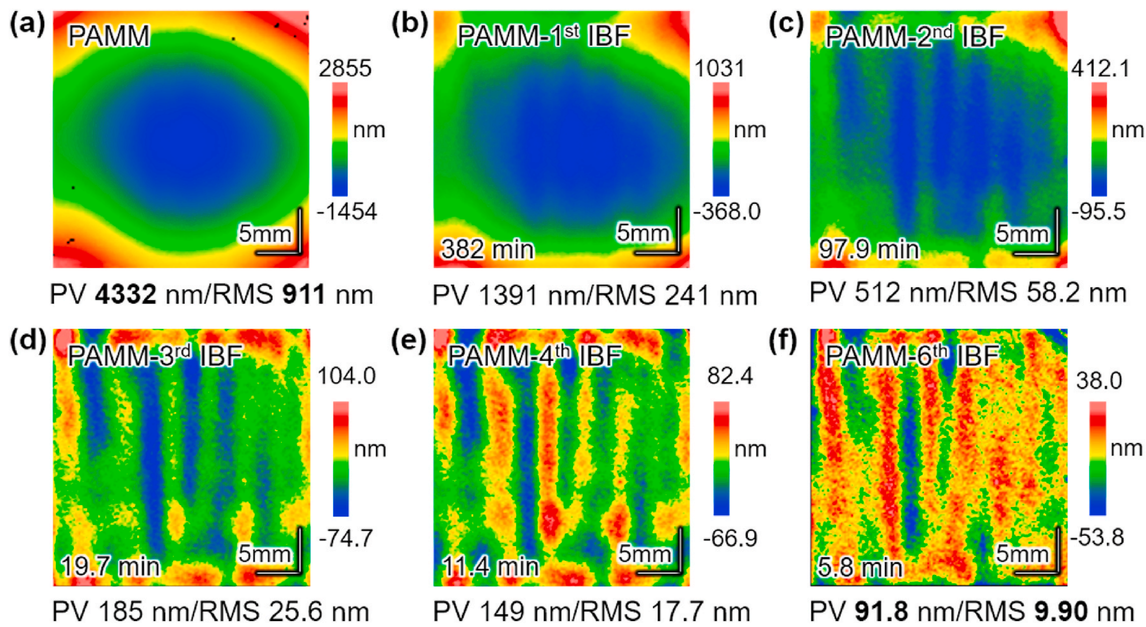

Fig. 6. The LI image, form error (PV, RMS) and processing time of the PAMM processed surface and subsequent IBF processed surface by different cycles.

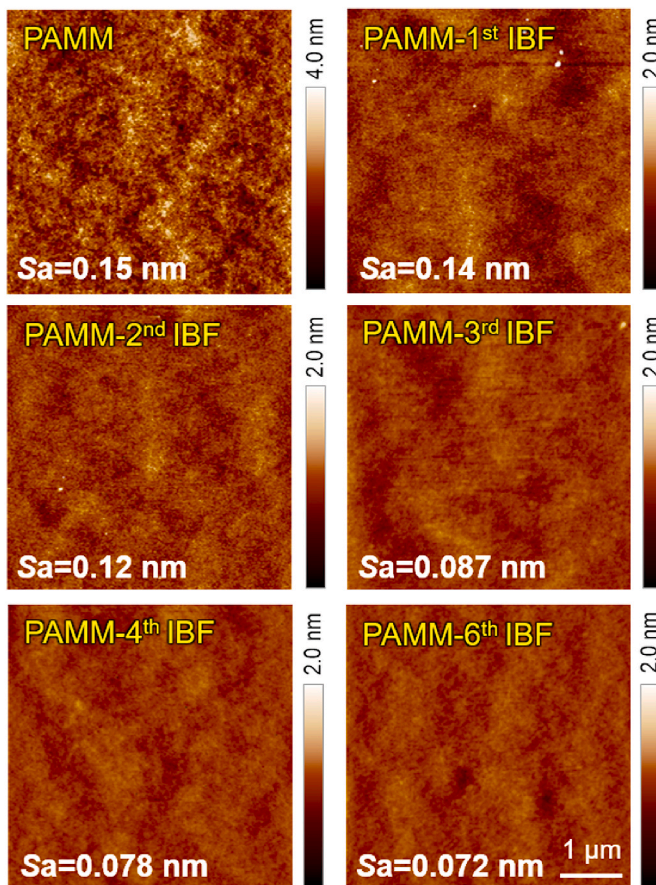

Fig. 7. The AFM images and *S*a roughness of the PAMM and subsequent IBF processed surface by different cycles.

3.3. PAMM-IBF of fused silica

To explore the effect of PAMM pre-processing on improving the surface quality of IBF processing, the evolution of LSF frequency error for the PAMM processed surface was studied under several IBF processing cycles. The LI images and form error (PV, RMS) for the surface after the cumulative processing of PAMM and the IBF with various cycles are shown in Fig. 6.

The form error of the original surface was similar to Fig. 4(a). As shown in Fig. 6(a), after PAMM, it can be found that PAMM induced significant form error on the surface, which increased the PV from 814 nm to 4.332 μm and the RMS from 194 to 911.8 nm within 12 min. When the atmospheric inductively coupled plasma irradiates the fused silica surface, the micro-melting materials in the central area may flow to the edge under airflow, forming a surface shape with a low center and a high periphery. On the other hand, the thermal stress induced by the high temperature of plasma seriously deteriorates the form error. Previous research showed obvious millimeter-scale low-spatial-frequency fluctuations on the PAMM-processed surface [35]. After 1st and 2nd cycles of processing of IBF, the form error on the PAMM processed surface was reduced to PV 512 nm and RMS 58.2 nm. However, the figuring duration of the 1st and 2nd cycles was 479.9 min, much larger than that of 44.1 min in Fig. 4(c). As shown in Fig. 6 (c), the ripples can be seen clearly, caused by the PAMM scanning process. Concerning the higher processing cycles of IBF, the convergence rate of form error decreases step by step. Further figuring for 19.7 min, the RMS was reduced to 25.6 nm after the 3rd IBF. Then, the RMS decreased to 17.7 nm for 11.4 min in the 4th IBF processing. The IBF processing time of the 6th cycle only consumed 5.8 min, and the RMS of the surface decreased to 9.90 nm. The width of the ripples was smaller than the full width at half maximum (FWHM) of the removal function, so it was difficult to remove by the 10 mm aperture.

The PAMM polished surface needs more processing time than the original surface due to the severely degraded form error. Also, the PAMM-IBF process converged the form error to about 10 nm, and the millimeter-scale ripples appeared on the surface. Thus, the deformation induced by PAMM can be removed by IBF with increasing figuring duration.

Fig. 7 shows the evolution of AFM morphology of PAMM processed surface and subsequent IBF processed surface by different cycles. PAMM has excellent smoothing ability, which realizes an atomic level ultra-smooth surface with a roughness of *S*a 0.15 nm. Meanwhile, the microscopic scratches on the original surface, as shown in Fig. 5, were recovered after PAMM. After the 1st IBF cycle on the PAMM processed

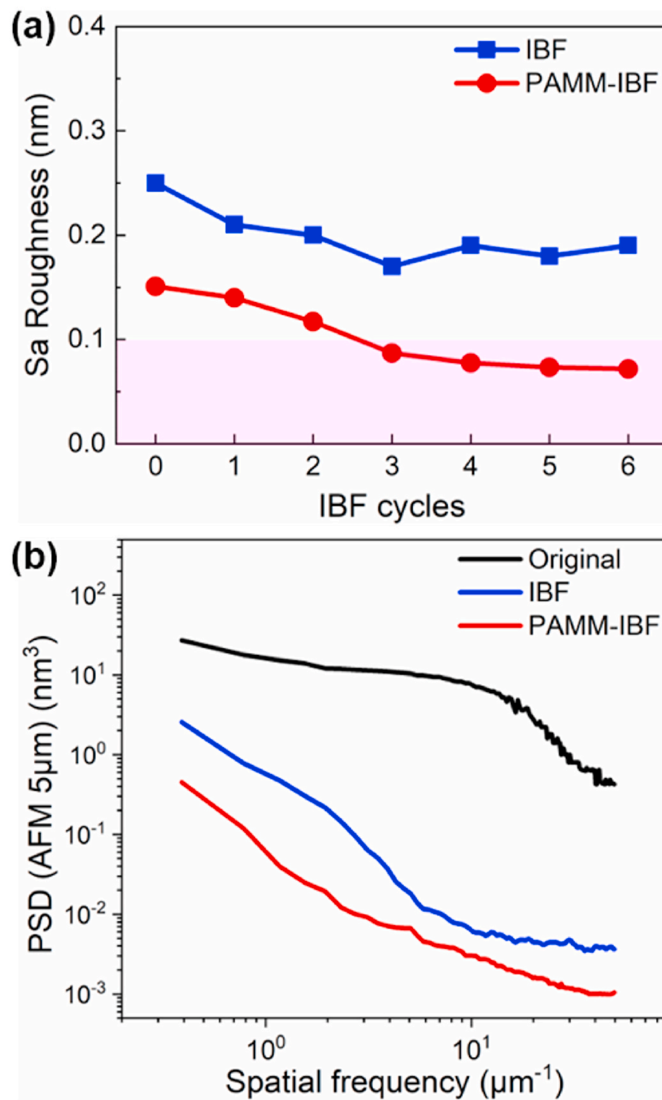

Fig. 8. (a) The evolution of the *S*a roughness (5 μm × 5 μm, by AFM). (b) PSD analysis of the original, IBF processed and PAMM-IBF processed surfaces.

sample, the *S*a roughness was decreased to 0.14 nm. After the 3rd cycle of IBF on the PAMM processed surface, the roughness further decreased to *S*a 0.087 nm, reaching the precision of sub-angstrom level. With the continuous IBF cycles, the roughness of the final surface was stabilized at *S*a 0.07 nm. With the progress of ion beam sputtering, the roughness convergence was close to the physical limit. It is demonstrated that ion beam figuring can simultaneously smooth the surface to sub-angstrom roughness when PAMM has recovered the surface defects.

The evolution of the *S*a roughness is shown in Fig. 8(a). As expected, PAMM improves the roughness of the original surface and enables IBF to obtain an atomically smooth surface. After the PAMM-IBF manufacturing process (over IBF 3 cycles), the *S*a roughness decreased to below 0.1 nm, which may be important for the reflecting performance of fused silica optics. For further investigation of the morphology evolution of the two samples, we take the power spectral density (PSD) analysis of the data from final AFM images in Figs. 5 and 7 for comparison. The surface errors within the measured frequency range are effectively removed during IBF and PAMM-IBF in Fig. 8(b). The PSD curve of IBF and PAMM-IBF were steeper than that of original. It indicated that IBF was more efficient in the higher frequency range. And the PSD curve of IBF processed was steeper than that of PAMM-IBF. This was because that the scratches and cracks cannot be removed by ion beam sputtering, while the higher frequency roughness can be smoothed quickly. The scratches evolved into micro pits and converted into the lower frequency errors.

The above results revealed the atomic-scale smoothing capability of PAMM-IBF during figuring. However, the removal depth and duration were different between IBF and PAMM-IBF process. To verify whether the roughness can be further optimized after IBF treatment with sufficient depth and duration, the uniform removal experiments were carried out. The original and PAMM-processed samples were scanned via ion beam at a constant speed, while kept all other parameters constant. The 40 × 20 mm^2 area of the substrate was scanned, and the other area was reference surface. The scan speed was 20 mm/min with 1 mm step pitch, and the duration was 37.4 min for one scan. Fig. 9(a) shows the uniform removal pattern after one scan. The removal depth was 1.07 μm from the removal profile in Fig. 9(b). Four uniform removal scans were carried out to compare the roughness evolution between IBF and PAMM-IBF process. Thus, the total removal depth was 4.28 μm, which was similar to the PV in Fig. 6(a). As shown in Fig. 9(c), the surface roughness decreased firstly and then stabled with the removal depth increasing during IBF process. After removal of 1.07 μm, the roughness decreased from 0.37 nm to 0.25 nm. Surface roughness was stabled at 0.22 nm after removal depth increased to 2.14 μm and 3.21 μm. The micro pits can be seen from the AFM image even if the removal depth increased up to 4.28 μm, and the *S*a roughness was still 0.22 nm. It was demonstrated that the micro pits, which were evolved from scratches, cannot be eliminated if the IBF treatment duration or removal depth increased. As for the PAMM-IBF process, the surface roughness decreased from 0.145 nm to 0.113 nm after removal of 1.07 μm. After removal of 2.14 and 3.21 μm, *S*a roughness decreased to 0.103 nm and 0.099 nm respectively. From the AFM image in Fig. 9(c), the roughness was decreased to 0.093 nm without micro pits after removal of 4.28 μm.

Compared to the IBF of the original surface, the PAMM-IBF process realized a smoother surface. It is assumed that the PAMM process benefits the following IBF process in two ways. Firstly, the migration of atoms during the PAMM process leads to an ultra-smooth surface. Secondly, the subsurface was reconstructed during the PAMM process. Thus, the subsurface damage can be recovered.

Although the PAMM-IBF process completed the polishing and figuring on the original surface of the fused silica sample, the LSF error was only reduced to about 10 nm, which needs further optimization. The millimeter-scale ripples were observed in the PAMM-IBF processed surface. The residual ripples on the PAMM-IBF processed surface in Fig. 6(f) were considered to be eliminated by using a smaller aperture of IBF. The new removal function (2 mm aperture) was applied in subsequent IBF finishing, as shown in the inset of Fig. 10(a). The FWHM is 2.7 mm, and the VRR is 1.1 × 10^{-3} mm^3/min. Fig. 10(a) shows the evolution of the PV, RMS of the figuring surface and its processing time during the subsequent IBF processing. The processing time of the 7th and 8th IBF cycles took about 4.5 h, and the form error of RMS reduced from around 10 nm–4 nm. The processing time for the 9th IBF cycle is 4.4 min, which means that the LSF error was close to the convergence limit. Fig. 10(b) shows the LI image of the final surface after subsequent IBF using a new removal function, and the significant residual millimeter-scale ripples in Fig. 6 were eliminated. The final form error was reduced to PV of 36.20 nm and RMS of 3.89 nm.

3.4. Evaluation of surface quality for the PAMM-IBF processed surface

Through the PAMM and continuous cycles of the IBF process with different removal footprints, the LSF error of the final formed surface converges to 3.89 nm. A comprehensive evaluation of error convergence is required at all spatial frequencies to evaluate the surface quality. Fig. 11(a) and (b) show the surface morphology and residual error information in different measurement ranges, which confirms that the roughness of *S*a for the final surface is finally reduced to the sub-nanometer level.

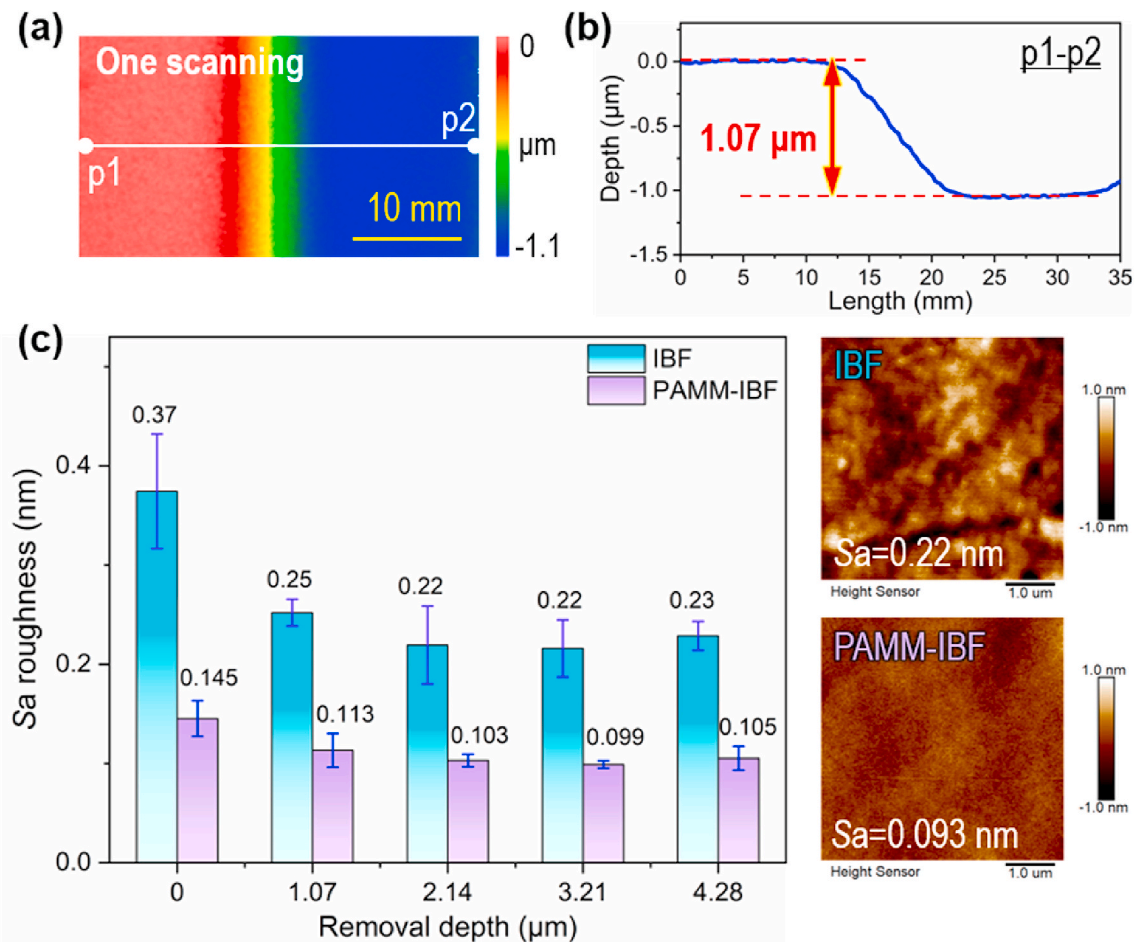

Fig. 9. Uniform removal pattern (a) and profile (b) after one scanning, roughness variation with different removal depth and AFM images of IBF and PAMM-IBF processes after removal of 4.28 μm (c).

The SWLI image shows the roughness reduced to 0.115 nm of MSF error. The AFM images show that the HSF error converges close to the physical limit (*Sa*: 0.044 nm) in Fig. 11(b). The AFM topography and SWLI topography data of the machined surface were extracted to calculate its PSD. The measured areas are 1 × 1 μm^2 and 20 × 20 μm^2 for AFM measurement and 400 × 400 μm^2 for SWLI measurement. The PSD results are shown in Fig. 11(c). The different spatial frequency errors of the fused silica surface were effectively reduced after the PAMM-IBF process.

Furthermore, the LSCM images of the PAMM-IBF finished, and BOE etched surfaces are shown in Fig. 12. After PAMM-IBF, the surface was very smooth. No etching pits were observed after BOE etching for 10 min, demonstrating the less damaged surface obtained by the proposed PAMM-IBF process. Thus, the PAMM-IBF realized an ultra-precision and ultra-smooth surface with less damage for fused silica. Full spatial frequency errors of the fused silica surface were effectively reduced, and nanometer-precision form accuracy and sub-angstrom roughness were obtained.

Fig. 13 summarizes the evolution mechanism of the IBF and PAMM-IBF processes, respectively. The scratches and SSD on the original surface would evolve into micro pits after ion beam sputtering. The surface and subsurface defects suppress the polishing effect of IBF because the micro pits cannot be removed completely by IBF. PAMM recovers the surface scratches and SSD, and an atomically smooth surface can be obtained. PAMM deteriorates the form error, but IBF can correct it. After PAMM pre-processing, IBF presents an excellent smoothing effect based on less damage and a smooth surface with *Sa* roughness of 0.044 nm was obtained. It means that the PAMM process enables IBF to obtain an ultrasmooth surface while achieving high-precision figuring. This atomically smoothing effect of IBF is essential for optical applications.

4. Conclusions

This paper proposed a process combining PAMM and IBF for obtaining ultra-precision surfaces with less damage of fused silica. The following conclusions can be drawn from this study.

- The IBF process can effectively reduce the form error from 193.8 nm to 8.86 nm RMS and the roughness of *Sa* from 0.25 nm to 0.19 nm. However, the scratches and SSD evolved into micro pits, limiting further roughness reduction.
- PAMM-IBF process was verified that the form error was reduced to 9.90 nm RMS and the roughness of *Sa* was reduced to 0.072 nm, which completed a sub-angstrom level breakthrough in surface roughness. Under the optimized removal function, the fused silica surface realized nanoscale precision of RMS 3.89 nm in LSF error, *Sa* 0.115 nm in MSF roughness and *Sa* 0.044 nm in HSF roughness, which completed the convergence of all spatial frequencies.
- By BOE detection, the PAMM process was proven to recover the defects on the CMP-processed surface/subsurface, and the PAMM-IBF process was proven not to introduce new defects. Therefore, the proposed PAMM-IBF was considered an efficient surface manufacturing process for fused silica surfaces with less damage.

The proposed PAMM-IBF has been proved for nanometer figure accuracy and atomically smooth surface with less damage. This approach

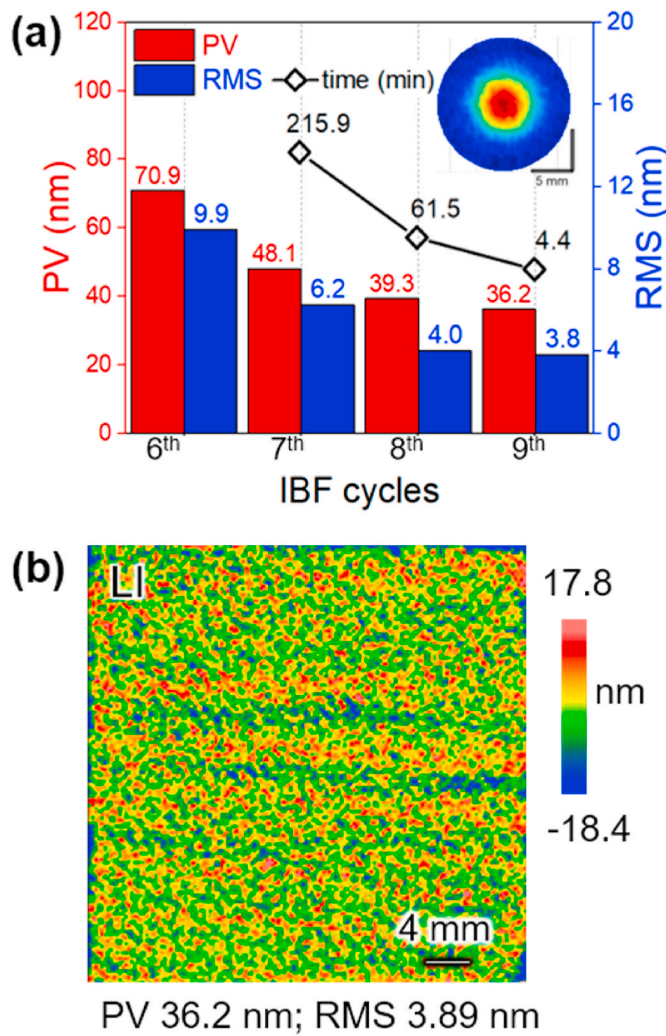

Fig. 10. (a) The evolution of the form error (PV, RMS) and processing time during the subsequent IBF cycles (Inset is the removal footprint with 2 mm aperture); (b) The LI image of the final surface after IBF using new removal footprint.

provides new possibilities for extreme manufacturing precision of optical surfaces and relevant applications with stringent requirements for less damage. The main hurdle for the practical application of this hybrid process is the thermal stress caused by high-temperature plasma. In the long run, the scan path, scan speed, and plasma ignition system will be optimized through experiments and simulations to compensate for uneven thermal distribution. Also, the annealing process can be employed to release the thermal stress after PMMA, thereby eliminating the thermal deformation.

CRediT authorship contribution statement

Bing Wu: Writing – original draft, Methodology, Investigation, Data curation. **Shaoxiang Liang:** Writing – original draft, Methodology, Data curation. **Junqi Zhang:** Methodology, Data curation. **Xuemiao Ding:** Methodology. **Tom Chiu:** Methodology. **Pei Huang:** Methodology, Investigation. **Yinhui Wang:** Writing – review & editing, Supervision, Methodology. **Hui Deng:** Writing – review & editing, Supervision, Methodology, Conceptualization.

Declaration of competing interest

The authors declare that they have no known competing financial

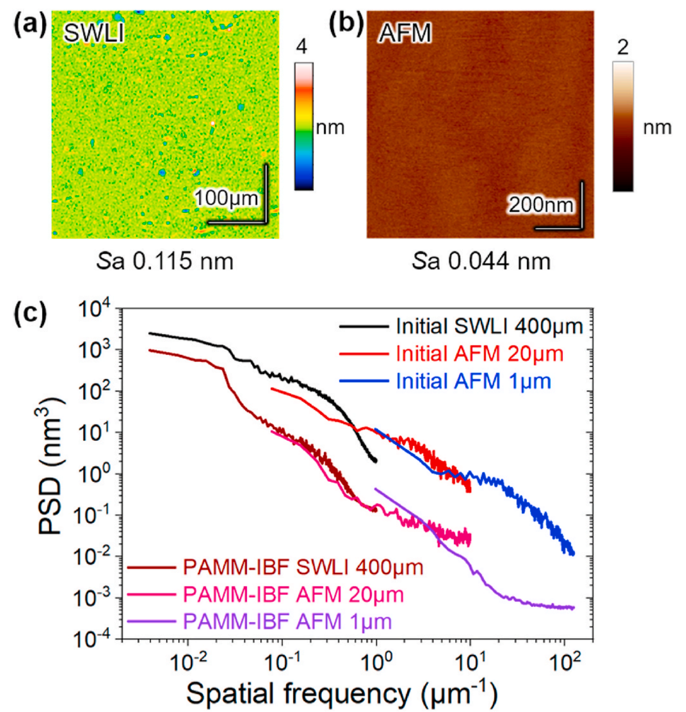

Fig. 11. The SWLI image (a) and AFM image (b) of the final PAMM-IBF processed surface; (c) PSD analysis of the original surface and PAMM-IBF processed final surface.

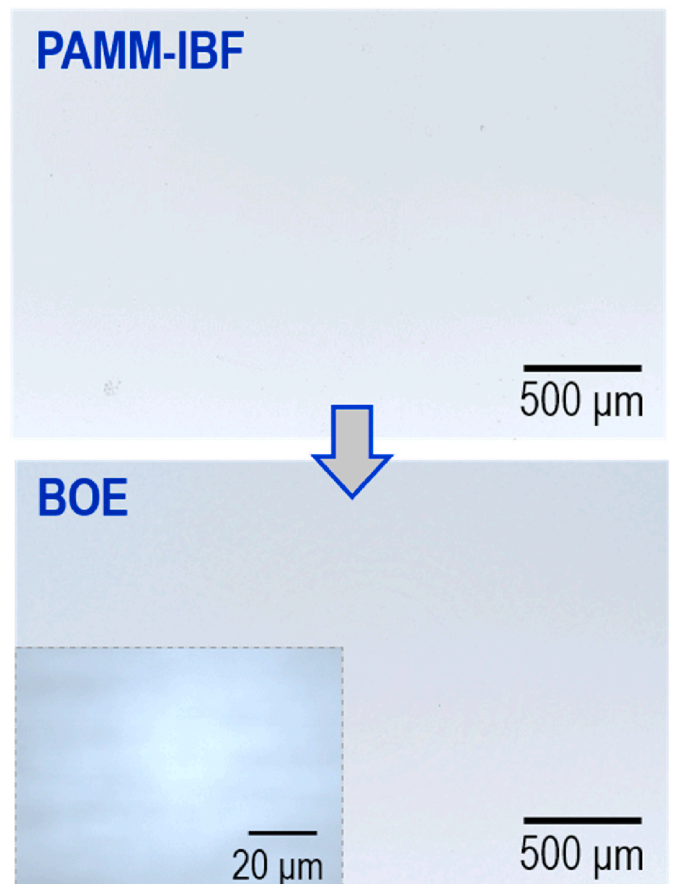

Fig. 12. LSCM morphology of fused silica of PAMM-IBF processed and subsequently dipped in BOE solution for 10 min.

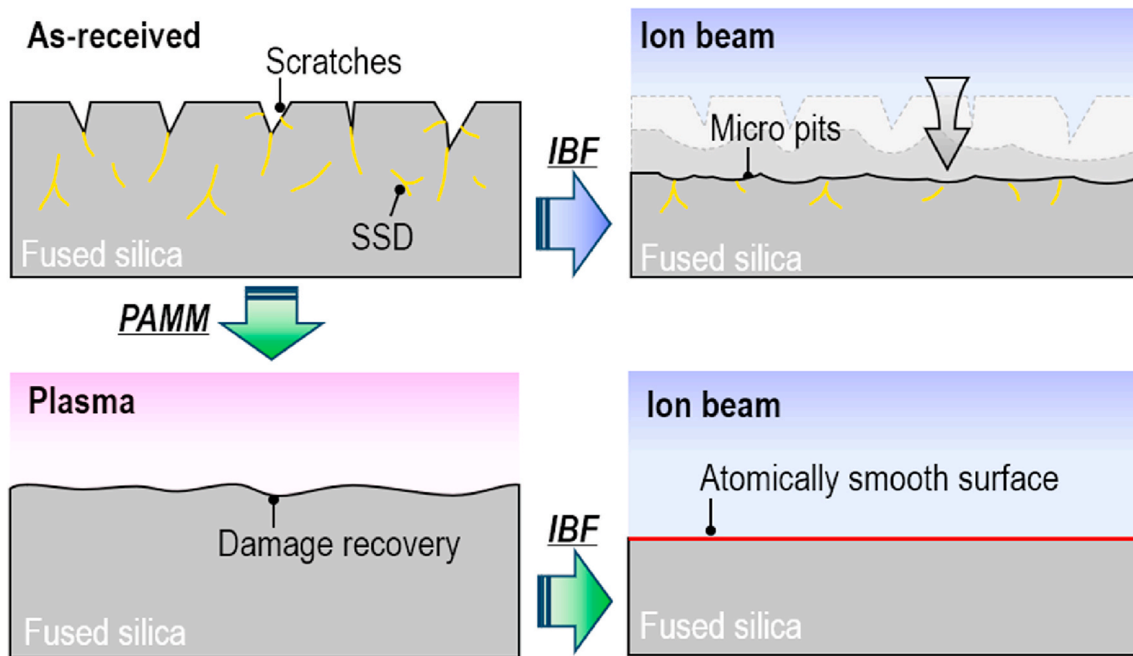

Fig. 13. Schematic for the evolution mechanism of IBF and PAMM-IBF processes.

interests or personal relationships that could have appeared to influence the work reported in this paper.

Acknowledgement

This work was supported by the National Natural Science Foundation of China (52375437, 52035009) and the Natural Science Foundation of Guangdong Province (2024B1515020027). The authors would like to thank the Shenzhen Science and Technology Program (Grant No. KQTD20170810110250357) for the financial support. The authors acknowledge the assistance of SUSTech Core Research Facilities. This work was also supported by Shenzhen Engineering Research Center for Semiconductor-specific Equipment.

References

[1] Ulrich W, Rostalski H-Jr, Hudyma R. Development of dioptric projection lenses for deep ultraviolet lithography at Carl Zeiss. J Nanolithogr MEMS, MOEMS 2004;3:87–96.
[2] Dai G, Hahm K, Sebastian L, Heidelmann M. Comparison of EUV photomask metrology between CD-AFM and TEM. Nanomanufacturing and Metrology 2022;5:91–100.
[3] Yumoto H, Mimura H, Koyama T, Matsuyama S, Tono K, Togashi T, et al. Focusing of X-ray free-electron laser pulses with reflective optics. Nat Photonics 2013;7:43–7.
[4] Wagner C, Harned N. Lithography gets extreme. Nat Photonics 2010;4:24–6.
[5] Taniguchi N. Current status in and future trends of ultraprecision machining and ultrafine materials processing. CIRP annals 1983;32:573–82.
[6] Glatzel H, Ashworth D, Bremer M, Chin R, Cummings K, Girard L, et al. Projection optics for extreme ultraviolet lithography (EUVL) micro-field exposure tools (METs) with a numerical aperture of 0.5. Extreme Ultraviolet (EUV) Lithography IV: SPIEL 2013:318–33.
[7] Hou X, Li J, Li Y, Tian Y. Intermolecular and surface forces in atomic-scale manufacturing. Int J Extrem Manuf 2022;4:022002.
[8] Lawson JK, Wolfe CR, Manes KR, Trenholme JB, Aikens DM, English Jr RE. Specification of optical components using the power spectral density function. Optical Manufacturing and Testing: SPIEL 1995:38–50.
[9] Débarre D, Booth MJ, Wilson T. Image based adaptive optics through optimisation of low spatial frequencies. Opt Express 2007;15:8176–90.
[10] Hudyma R, Sommargren GE, Sweeney DW, Taylor J. Fabrication and testing of optics for EUV projection lithography. Livermore, CA (United States): Lawrence Livermore National Lab.(LLNL); 1998.
[11] Endo H, Inaba T, Pahlovy SA, Miyamoto I. Low energy Xe+ ion beam machining of ULE® substrates for EUVL projection optics–Evaluation of high-spatial frequency roughness. Microelectron Eng 2010;87:982–4.
[12] Matsuzawa Y, Hiraguri K, Hashizume H, Mimura H. Organic abrasive machining system for optical fabrication with 0.1-mm spatial resolution. Rev Sci Instrum 2022;93.
[13] Golini D, Dumas P, Kordonski W, Hogan S, Jacobs S. Precision optics fabrication using magnetorheological finishing. Optical fabrication and testing. Optica Publishing Group; 1998. OMD. 1.
[14] Yamauchi K, Mimura H, Inagaki K, Mori Y. Figuring with subnanometer-level accuracy by numerically controlled elastic emission machining. Rev Sci Instrum 2002;73:4028–33.
[15] Beaucamp A, Namba Y. Super-smooth finishing of diamond turned hard X-ray molding dies by combined fluid jet and bonnet polishing. CIRP annals 2013;62:315–8.
[16] Weiser M. Ion beam figuring for lithography optics. Nucl Instrum Methods Phys Res Sect B Beam Interact Mater Atoms 2009;267:1390–3.
[17] Gu Q, Zhang Z, Zhou H, Yu J, Wang D, Feng J, et al. A novel approach of jet polishing for interior surface of small-grooved components using three developed setups. Int J Extrem Manuf 2024;6:025101.
[18] Arnold T, Pietag F. Ion beam figuring machine for ultra-precision silicon spheres correction. Precis Eng 2015;41:119–25.
[19] Zhou L, Dai Y, Xie X, Li S. Optimum removal in ion-beam figuring. Precis Eng 2010;34:474–9.
[20] Wang T, Huang L, Zhu Y, Giorgio S, Boccabella P, Bouet N, et al. Ion beam figuring system for synchrotron X-ray mirrors achieving sub-0.2-μrad and sub-0.5-nm root mean square. Nanomanufacturing and. Metro 2023;6:20.
[21] Völlner J, Ziberi B, Frost F, Rauschenbach B. Topography evolution mechanism on fused silica during low-energy ion beam sputtering. J Appl Phys 2011;109.043501–6.
[22] Li C, Hu Y, Wei Z, Wu C, Peng Y, Zhang F, et al. Damage evolution and removal behaviors of GaN crystals involved in double-grits grinding. Int J Extrem Manuf 2024;6:025103.
[23] Liao W, Dai Y, Liu Z, Xie X, Nie X, Xu M. Detailed subsurface damage measurement and efficient damage-free fabrication of fused silica optics assisted by ion beam sputtering. Opt Express 2016;24:4247–57.
[24] Xu M, Dai Y, Zhou L, Peng X, Chen S, Liao W. Evolution mechanism of surface roughness during ion beam sputtering of fused silica. Appl Opt 2018;57:5566–73.
[25] Savvides N. Surface microroughness of ion-beam etched optical surfaces. J Appl Phys 2005;97.
[26] Neauport J, Ambard C, Cormont P, Darbois N, Destribats J, Luitot C, et al. Subsurface damage measurement of ground fused silica parts by HF etching techniques. Opt Express 2009;17:20448–56.
[27] Cui X, Zhang Z, Yu S, Chen X, Shi C, Zhou H, et al. Unprecedented atomic surface of silicon induced by environmentally friendly chemical mechanical polishing. Nanoscale 2023;15:9304–14.
[28] Xu J, Chen G, Qiao J, Lambropoulos JC. Assessment of sub-micron subsurface damage in glass. Appl Opt 2023;62:4161–70.
[29] Liang H, Wei Z, Fang J, Li Y, Li C, Xie Z, et al. Electrolyte effect on photoetching of gallium nitride. Nanomanufacturing and Metrology 2024;7:5.
[30] Xu G, Zhang Z, Meng F, Liu L, Liu D, Shi C, et al. Atomic-scale surface of fused silica induced by chemical mechanical polishing with controlled size spherical ceria abrasives. J Manuf Process 2023;85:783–92.

[31] Liang S, Zhang L, Deng H. Theoretical and experimental study on plasma-induced atom-migration manufacturing (PAMM) of glass. Appl Surf Sci 2022;599:153976.
[32] Li R, Li Y, Deng H. Plasma-induced atom migration manufacturing of fused silica. Precis Eng 2022;76:305–13.
[33] Jones RA. Optimization of computer controlled polishing. Appl Opt 1977;16:218–24.
[34] Wu JF, Lu ZW, Zhang HX, Wang TS. Dwell time algorithm in ion beam figuring. Appl Opt 2009;48:3930–7.
[35] Liang S, He Y, Ding P, Wang C, Guo L, Deng H. Smoothing of fused silica with less damage by a hybrid plasma process combining isotropic etching and atom-migration. Surface Interfac 2023;41:103191.